Journal of Materials Chemistry A

ROYAL SOCIETY OF CHEMISTRY

PAPER

Cite this: *J. Mater. Chem. A*, 2020, **8**, 7756

Design principles of pseudocapacitive carbon anode materials for ultrafast sodium and potassium-ion batteries†

Yong Gao,[a] Jing Zhang,[a] Nan Li,[a] Xiao Han,[a] Xian Luo,[a] Keyu Xie,[a] Bingqing Wei [b] and Zhenhai Xia *[c]

Received 15th February 2020
Accepted 30th March 2020

DOI: 10.1039/d0ta01821j

rsc.li/materials-a

Sodium- and potassium-ion batteries are one of the most promising electrical energy storage devices at low cost, but their inferior rate and capacity have hampered broader applications such as electric vehicles and grids. Carbon nanomaterials have been demonstrated to have ultrafast surface-dominated ion uptake to drastically increase the rate and capacity, but trial-and-error approaches are usually used to find desired anode materials from numerous candidates. Here, we developed guiding principles to rationally screen pseudocapacitive anodes from numerous candidate carbon materials to create ultrafast Na- and K-ion batteries. The transition from pseudocapacitive to metal-battery mechanisms on heteroatom-doped graphene in charging process was revealed by the density functional theory methods. The results show that the graphene substrate can guide the preferential growth of K and Na along graphene plane, which inhibits dendrite development effectively in the batteries. An intrinsic descriptor is discovered to establish a volcano-shaped relationship that correlates the capacity with the intrinsic physical qualities of the doping structures, from which the best anode materials could be predicted. The predictions are in good agreement with the experimental results. The strategies for enhancing both the power and energy densities are proposed based on the predictions and experiments for the batteries.

Introduction

Sodium ion batteries (SIBs), as a promising alternative to lithium ion batteries (LIBs), have received extensive attention recently because sodium exhibits excellent electrochemical properties similar to those of lithium in the same alkali group and has abundant resources with a cost 40 times lower than that of lithium.[1–5] Various cathode materials including transition metal oxides ($NaCoO_2$ and $NaxMnO_2$), phosphates ($NaMPO_4$ (M = Fe, Mn, Co, *etc.*)), and fluorides ($NaMF_3$ (M = Ni, Fe, Mn)) have been developed and proved to exhibit comparable performance to lithium-ion batteries.[6–10] However, the design of anode materials with high rate capability and capacity, superior reliability and safety, and long cycle life has always been a major scientific challenge,[11] which directly restricts the comprehensive performance of ion full batteries.

Considering the similarity of the working mechanism between the two kinds of batteries, until now, following the design concepts for anode materials of LIBs, many ion diffusion-controlled anode materials for SIBs (Table S1, ESI†) have been developed including carbon materials such as graphite,[12] carbon fibers,[13] and acetylene black,[14] Na-alloys like $Na_{15}Ge_4$,[15] $Na_{15}Sn_4$,[16] $Na_{15}Pb_4$,[17] Na_3P,[18] and Na_3Sb,[19] and even bifunctional hybrids made by incorporating alloys into the graphene backbone.[20] Although these materials significantly improve the capacity of SIBs, they all have a common weakness—low rate capability—owing to slow ion diffusion in bulk host materials due to the deintercalation/intercalation process laboriously caused by the smaller interlayer distance and huge volume expansion of the electrode originating from the alloying reaction. In fact, the above problems in SIBs are more severe than those in LIBs as a sodium ion has a larger radius (1.02 Å) and higher molar mass (23), requiring a layer spacing of at least 3.7 Å for reversible deintercalation/intercalation, which inevitably gives rise to a poor diffusion rate in the bulk electrode and considerable technical difficulty for designing such anode materials. Other emerging ion-based batteries such as potassium ion batteries (KIBs),[21] calcium ion batteries (CaIBs),[22] zinc ion batteries (ZIBs),[23] and aluminium ion batteries (AlIBs),[24] face similar challenges in the design of anode materials.

[a]*State Key Laboratory of Solidification Processing, School of Materials Science and Engineering, Northwestern Polytechnical University, Xi'an, Shaanxi 710072, China*

[b]*Department of Mechanical Engineering, University of Delaware, Newark DE 19716, USA*

[c]*Department of Materials Science and Engineering, Department of Chemistry, University of North Texas, Denton, TX 76203, USA. E-mail: Zhenhai.xia@unt.edu*

† Electronic supplementary information (ESI) available. See DOI: 10.1039/d0ta01821j

To overcome the challenges, one promising route for the design of anode materials is to use capacitive process-controlled materials instead of traditional ion diffusion-controlled materials. While enhancing the ion transportation in bulk electrodes, this approach would avoid various shortcomings such as volumetric expansion and severe interlayer width. Along these lines, there have been several reports on anode materials that operate to achieve a high rate in the pseudocapacitive mechanism for storage of sodium ions (Table S1, ESI†), including graphene-based nitrogen-doped carbon sandwich nanosheets,[25] hierarchical layered graphene composites,[26] and ferroelectric $Sn_2P_2S_6$ with layered nanostructures with pseudocapacitive sodium storage.[27] Among them, the heteroatom-doping technique has attracted more attention for the improvement of the capacity and rate of the carbon anode, particularly capacitive process-controlled carbon anodes in SIBs. It has been demonstrated that heteroatom dopants (*e.g.*, N, B, S, P, or F) can significantly enhance both capacity and rate capability of carbon-based SIBs (Table S2, ESI†).[28–32]

Despite the potential of heteroatom-doped carbon nanomaterials for ultrafast SIBs, trial-and-error approaches are still used for the development of SIBs. To rationally design effective anode materials for the ultrafast SIBs, it is necessary to correlate the doping structures with the capacity of the carbon-based anode. Some work has been done by using the first-principles calculations to understand the energy storage mechanisms and to estimate the charge storage ability of heteroatom-doped carbon electrodes.[33–35] For the entire family of metal-free carbon-based electrodes, however, there lacks design principles or intrinsic descriptors that govern charge storage activities of Na and K ion batteries.

Herein, the graphene structures doped with p-block elements in the periodic table are used as anode materials for SIBs and KIBs for sodium and potassium ion storage. The capacity C and rate capability P are correlated with the heteroatom-doped structures of carbon nanomaterials by an intrinsic descriptor that can be used for screening the best electrode materials. The predictions are consistent with the experimental results. The results reveal the transition from the capacitive mechanism to the phase reaction mechanism in the process of sodium and potassium ion storage, from which the design principles are established for enhancing both capacity and rate capability of carbon-based anode materials for SIBs and KIBs simultaneously. The results provide a theoretical base for searching for the desired carbon-based anode materials for ultrafast SIBs and KIBs.

Results

Mechanism and origin of heteroatom-doped graphene for Na^+ and K^+ storage

Active sites for Na^+ and K^+ storage in heteroatom-doped carbon. Graphene doped with p-block elements X (X = B, Si, N, P, Sb, O, S, F, Cl, Br, and I) as an anode was modeled, as shown in Fig. 1a and S1 (ESI†). The doping density of the models is 1.8 at% for zigzag graphene, 2.1 at% for graphene nanosheets, and 2.8 at% for the armchair graphene model and

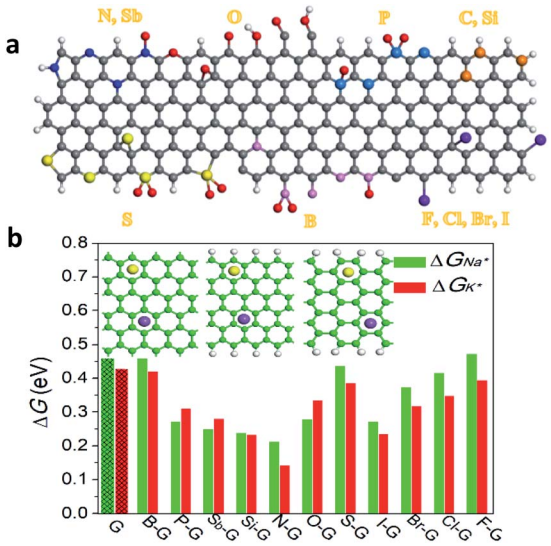

Fig. 1 (a) Summary of the heteroatom doping modes: (top row, from left to right) pr-N(Sb), py-N(Sb), g-N(Sb), N(Sb)–O, py-O, C–O–C, C=O, C–OH, C–C=O, C–C–OH, P–3C–O, P–3C, 2P–2C–2O, P–2C, g-C(Si), z-C(Si) and a-C(Si); (bottom row, from left to right) th-S, py-S, C–S–C, S–2O, th-S-2O, B–3C, C–B–2O, B=C, B–2C, B–2C–O, z-(F, Cl, Br, and I), g-(F, Cl, Br, and I) and a-(F, Cl, Br, and I); orange/grey, blue, pink, light cadet blue, yellow, red, purple, and white balls represent C(Si), N(Sb), B, P, S, O, F (Cl, Br, I), and H atoms, respectively. (b) Bar graph of computed minimum positive Gibbs free energy ΔG_{Na^*} and ΔG_{K^*} at $U = 0$ and the insets represent the hollow sites adsorbing Na and K for different graphene structures (from left to right: inplane, zigzag-edged and armchair-edged graphene, and green, white, yellow and purple balls in these graphene structures represent C, H, Na and K, respectively).

is similar to that in the experiments. Upon charging, sodium ions in a neutral electrolyte (0.5 M Na_2SO_4) or potassium ions in an alkaline electrolyte (6 M KOH) driven by an external electric potential U are chemisorbed on the sites of the anode surface to combine electrons from the external circuit through the reaction:

$$C^+ + e^- + * \underset{\text{Discharging}}{\overset{\text{Charging}}{\rightleftharpoons}} C^* \quad (1)$$

where * denotes the sites of the doped graphene electrode and C^+ and C* are the dissociative sodium or potassium ions in the electrolyte and those chemisorbed on the electrode, respectively. The discharge process is the reverse reaction of eqn (1), in which chemisorbed sodium or potassium ions desorb from the anode surface.

To identify active sites for ion storage, the chemical adsorption energy ΔG_{C^*} of the ions at all possible sites of the doped graphene was calculated. The adsorption positions of sodium and potassium atoms on doped/pure graphene models, together with the adsorption energy, are shown in Fig. S2–S5 (ESI†). Unlike the protons that are directly adsorbed on the carbon atoms in the capacitors,[36] sodium and potassium occupy the hollow positions of the graphene due to their relatively large size, as shown in the inset of Fig. 1b. The chemical adsorption energy ΔG_{C^*} is distributed unevenly on different positions due

to the edge and doping effects, as shown in Fig. S5 and S6 (ESI†). In the charge process, cations (Na^+ or K^+) may first adsorb on the sites with the lowest chemical adsorption energy ΔG_{C*} (ΔG_{Na*} and ΔG_{K*}) due to their the lowest energy barrier. These sites serve as the starting point of the whole charge process. The ions will then be deposited on the positions with the second lowest adsorption energy, and this process successively continues till all the positions are occupied. After all the positions are filled, the ions could further be deposited on the surface of the adsorbed ion layer.

Although all the positions could be occupied in the charge process, not all adsorbed ions can be released during discharging. Specifically, only those ions adsorbed at the sites with $\Delta G_{C*} > 0$ can be released to electrolytes. Thus, according to the values of ΔG_{C*} and ion deposition positions the sites can be divided into three categories: (i) irreversible adsorption sites ($\Delta G_{C*} < 0$), (ii) reversible adsorption sites ($0 < \Delta G_{C*} < \Delta G_T$), and (iii) stacking sites ($\Delta G_{C*} > \Delta G_T$), where ΔG_T is the free energy of phase transition (atom stacking). For the irreversible adsorption sites, since the adsorption energy is negative ($\Delta G_{C*} < 0$), ions can chemisorb on them spontaneously but cannot desorb during discharging. Hence the ions on these sites are ineffective and have no contribution to the charge storage. In the case of the reversible charge storage sites with $\Delta G_{C*} > 0$, the adsorbed ions (Na^+ or K^+) could be spontaneously released during discharging. However, when $\Delta G_{C*} > \Delta G_T$, nucleation and growth of the bulk metallic sodium or potassium phase could occur. This marks the transition from the pseudocapacitive mechanism in supercapacitors to the metal deposition mechanism existing in lithium-, sodium- and potassium-metal batteries.

Since only the sites with $\Delta G_{C*} > 0$ are the active sites for charge storage, the minimum positive chemical adsorption ΔG_{C*}^{min} is important and can be considered as an indicator of effective ion storage on the heteroatom-doped carbon electrode surface. ΔG_{C*}^{min} for pristine and doped graphene structures was calculated and is shown in Fig. 1b.

Transition from the surface-induced pseudocapacitive mechanism to the metal battery mechanism for Na^+/K^+ storage. As mentioned above, ions will be deposited successively on the active sites of the graphene, and in this process the energy for depositing atoms will be different due to the edge and doping effects as well as the interaction between the adsorbed ions and deposited ions. We have simulated the ion deposition (charging) process on pristine and doped graphene structures (Fig. 2a) and further calculated the chemical adsorption energy ΔG_{Na*} for each site. Fig. 2b shows the dependence of adsorption energy ΔG_{Na*} on the amount of chemisorbed Na^+ (or the coverage θ) for all heteroatom-doped graphene substrates including pure graphene. At the beginning of the deposition, ΔG_{Na*} increases almost linearly with increasing the number of chemisorbed ions and then gradually reaches a plateau. Similar deposition features were also found in doped graphene electrode structures with defects, as shown in Fig. S8 (ESI†). The increased adsorption energy can be attributed to the increased lateral repulsive interaction resulting from more sodium ions adsorbed on the surface. In addition, sodium ions adsorbed on the anode surface gradually rearrange to form a more regular

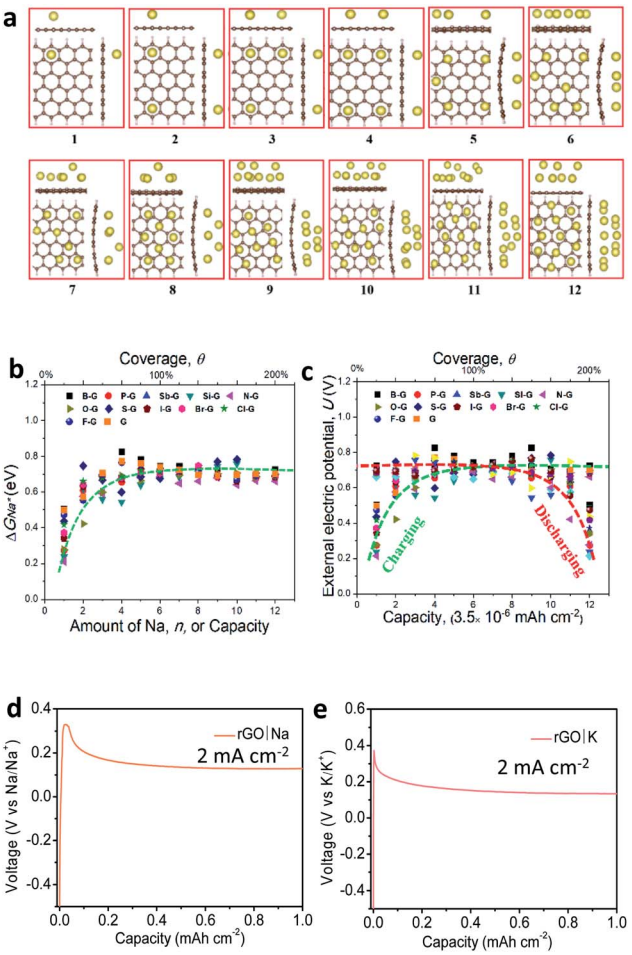

Fig. 2 (a) Structural evolution upon sodium atom deposition on the z-C graphene model. The numbers from 1 to 12 refer to the number of ions deposited on the surface of graphene. (b) External electric potential U (*vs.* Na^+/Na) *versus* amount of Na chemisorbed on the optimal p-block element doped graphene models (or coverage, θ). (c) External electric potential U (*vs.* Na^+/Na) *versus* capacity on the optimal p-block element doped graphene models (or coverage, θ) for the charge and discharge process. (d) Profiles of voltage *vs.* capacity for Na deposition on rGO at 2 mA cm^{-2}. (e) Profiles of voltage *vs.* capacity for K deposition on rGO at 2 mA cm^{-2}.

monolayer with the increase of sodium ions adsorbed on the substrate, as illustrated in Fig. 2a. Obviously, the topological structure of the monolayer is strongly affected by the topological structure of the graphene substrate.

After the monolayer is formed or even before the graphene surface is completely covered ($\theta = 100\%$), ions start to deposit on top of the monolayer and the second deposition layer merges, as shown in Fig. 2a. In this stage of ion deposition as observed in lithium-, sodium- and potassium-metal batteries, the adsorption energy ΔG_{Na*} becomes constant after $\theta > 100\%$, as shown in Fig. 2b, corresponding to the constant charge/discharge electric potential, as shown in Fig. 2c. Thus, from the adsorption energy and deposition coverage changes, it is clear that charging involves an initial ion adsorption in capacitive mechanism, followed by metal-multilayer formation in metal-battery mode.

For potassium ion (K^+) storage, almost the same mechanism was also demonstrated, as shown in Fig. 3. However, compared with sodium ions (Na^+), there are two key differences: (i) higher free energy of phase transition ΔG_T, which was also demonstrated by our electrochemical test and (ii) more potassium deposition in the monolayer. As illustrated in Fig. 2a and 3a, for the same substrate with the same area, upon the 7th sodium atom deposition on the substrate, phase transition occurs with the growth of the second sodium layer, while for potassium deposition, the second potassium layer does not start to grow until the 11th potassium atom is chemisorbed. The difference is mainly ascribed to the stronger adsorption binding of graphene to potassium ions, and hence the doped graphene electrodes are capable of storing more potassium ions based on the capacitive mechanism compared with sodium ion storage.

To experimentally demonstrate this transition mechanism predicted from the DFT calculation, Na and K ion batteries were prepared using Na and K plating/stripping on reduced graphene oxide (rGO) electrodes and a charging experiment was performed (see details in Methods). The results showed that the change of external electric potential *U versus* capacity *C* for both Na and K deposition consists of two parts, a linear increase and a plateau, as illustrated in Fig. 2d and e, which is in good agreement with our DFT predictions. The predicted trend of potential *U versus* capacity *C* is also in line with the capacitive characteristics, as shown in Fig. S7 (ESI†). In addition, the negative electric potential *U* for charging in experiments originates from negative irreversible adsorption sites resulting from defects of the rGO anode, as demonstrated in DFT calculation.

In Na-/K-metal batteries, one of the big issues is the inevitable growth of dendritic Na and K during cycling, which usually results in low coulombic efficiencies, internal short circuits, unnecessary waste of Na and K metals, and even catastrophic cell failures. This would cut down the energy and power densities of full battery cells and hinder their commercialization.[37] We have further simulated the growth of K and Na bulk metals on the graphene surface. As observed in Fig. 4b–d, the metals grow along a certain direction of the graphene in a plane manner of layer by layer growth while the external electric potential still remains stable (Fig. 4a). The orientation and topological structures of the bulk metals are very similar to the preferred growth of lithium ions on the graphene substrate, as observed in the experiments. Specifically, as illustrated in Fig. 4c and d, the first two layers of potassium and sodium atoms in the bulk potassium and sodium metal phase orientate in a certain angle on graphene nanoribbons. Both K and Na atoms on the graphene distribute like those in the (110) plane in a BCC structure. The K [111] and Na [111] directions are parallel to the zigzag edge of graphene (Fig. 4c and d). Interestingly, the (110) spacings of K (3.762 Å) and Na (3.034 Å) are approximately 1.5 and 1.2 times the length of one carbon hexagon (2.478 Å) along the graphene zigzag direction. These orientation and topological matches between the metal and substrate would indicate a preferential growth of metals on the substrate. In general, if lattice mismatch δ is 5%, the corresponding surfaces

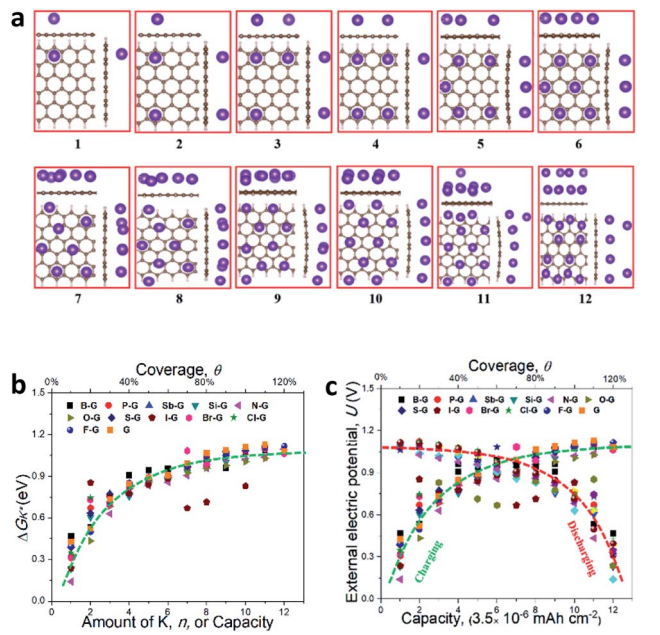

Fig. 3 (a) Structural evolution upon potassium atom deposition on the z-C graphene model. The numbers from 1 to 12 refer to the number of ions deposited on the surface of graphene. (b) ΔG_{K*} *versus* the amount of K chemisorbed on p-block element doped graphene models (or coverage, θ). (c) External electric potential *U* (*vs.* K/K^+) *versus* the capacity of p-block element doped graphene models (or coverage, θ) for the charge and discharge processes.

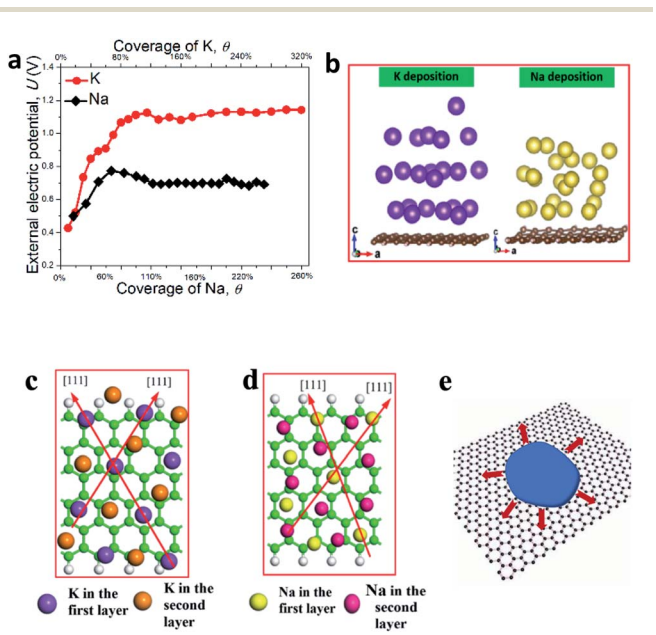

Fig. 4 (a) The external electrical potentials *versus* coverage (θ) of Na and K chemisorbed on zigzag graphene models. (b) Multilayered bulk phase structure of K and Na deposited on substrates. (c) Distribution and orientation of the first two layers of potassium atoms on the z-C model. (d) Distribution and orientation of the first two layers of sodium atoms on the z-C model. (e) Schematic of planar growth of sodium and potassium on the surface of graphene.

of two phases can be coherent. We have calculated the lattice mismatches of Na, K, and Li with the graphene substrates (Table S3†) according to the formula of lattice mismatch,

$$\delta = \frac{a_s - n \times a_N}{a_N},$$

where a_s and a_N are the spacings of the substrate and crystal nucleus atoms, respectively, and n represents the multiplier factor. The lattice mismatches with the graphene for K and Na are 1.82% and 2.44%, respectively. Such small lattice mismatches may lead to the epitaxial alignment between the planar K and Na and graphene. These simulation results indicate that the graphene substrate can guide the preferentially planar growth of K and Na during the long-term and repeated electrodeposition process (Fig. 4e). While the rate and capacity could be significantly enhanced, this planar growth could inhibit dendrite development effectively in potassium- and sodium-batteries.[39] Although the above prediction has not been confirmed experimentally, lithium batteries did show guided growth of planar Li layers, instead of random Li dendrites, on self-assembled reduced graphene.[38] The graphene substrate still exhibits the planar Li feature after 100 cycles while there is severe dendritic Li growth on the Cu foil. This experimental result demonstrates the long-term stability of the graphene-guided directional growth of the planar layers of Li, and possibly K and Na.

Design principle of heteroatom-doped carbon-based pseudocapacitive anode materials

An effective strategy for rationally designing an anode material is to establish a direct correlation between the intrinsic descriptor of the material and its specific capacitance C or energy density E. In our previous work,[36,40] we showed that the active sites of the doped graphene structures were correlated with a descriptor: the intrinsic physical properties of dopants, electronegativity E_X and electron affinity A_X by

$$\varnothing = \frac{E_X A_X}{E_C A_C} \quad (2)$$

where E_X and A_X are the electronegativity and electron affinity of heteroatoms, respectively, and E_C and A_C are the electronegativity and electron affinity of carbon, respectively. On the other hand, in the case of surface-dominated anodes uptaking sodium and potassium ions during the electrochemical process, our simulation results show that the minimum adsorption energy ΔG_{C*}^{min} is important and related to the specific capacitance $C_{0/site}$ (unit, e V^{-1}) in the range of $\Delta G_{C*}^{min} < eU < \Delta G_{C*}^{max} = \Delta G_T$ by[36]

$$C_{0/site} = \frac{\frac{1}{2}e^2\left(\frac{eU - \Delta G_{C*}^{min}}{\Delta G_{C*}^{max} - \Delta G_{C*}^{min}}\right)^2}{\frac{eUk_BT}{eU - \Delta G_{C*}^{min}} \ln\left[\frac{1}{2}\left(1 + e^{\frac{eU - \Delta G_{C*}^{min}}{k_BT}}\right)\right]} \quad (3)$$

where U is the external potential, e and k_B are the charge of an electron and Boltzmann constant, respectively, and ΔG_{C*}^{min}, ΔG_{C*}^{max} and ΔG_T are the minimum positive free energy, the maximum free energy and the free energy of phase transition (see details in the ESI†), respectively. According to eqn (3), the specific capacitance increases sharply with reduction of ΔG_{C*}^{min}, and this analytical result from eqn (3) is consistent with the DFT calculation, as shown in Fig. 5a.

We have correlated the minimum positive free energy ΔG_{C*}^{min} and the specific capacitance with the descriptor. Since the phase transition energy ΔG_T is about 1 eV and 0.7 eV for potassium and sodium ion adsorption, respectively, the potential U in eqn (3) was set to 1 V and 0.7 V to calculate the specific capacitance for KIBs and SIBs. Fig. 5b and c show the minimum positive free energy and the specific capacitance as a function of the descriptor $\varnothing$, respectively. Obviously, there are dual volcano relationships with N-doping and I-doping at the peaks (Fig. 5c), which correspond to two minima of the curve in Fig. 5b. Therefore, N-doped graphene stands out among the p-block element doped materials as the best anode material.

To verify the volcano relationship predicted by the descriptor $\varnothing$, relevant experimental data were cited from the literature, as listed in Tables S6 and S7.† To reliably compare the measured specific capacitances with our predictions, first, all the experimental data cited in this work were selected under the same conditions: the same alkaline electrolyte (KOH) and neutral electrolyte (Na_2SO_4). Secondly, all experimental data obtained were on the basis of the capacitive charge storage mechanism, avoiding the contribution from other charge storage mechanisms. Finally,

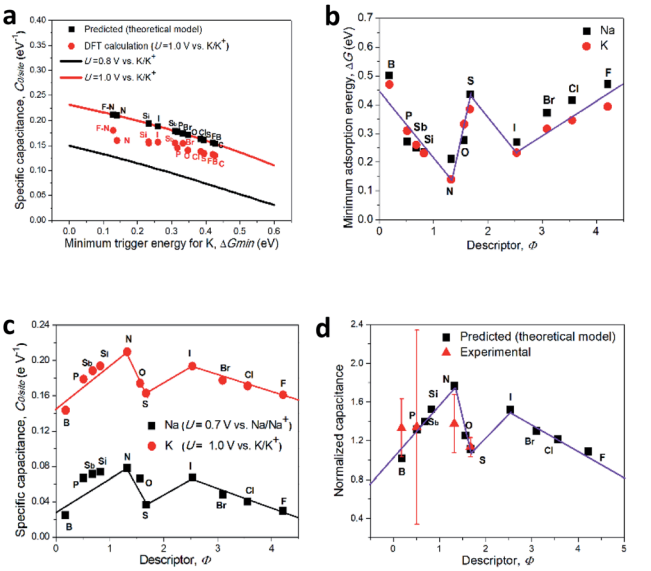

Fig. 5 (a) The capacitance of the unit charge storage site *versus* minimum Gibbs free energy at $U = 0.8$ and 1.0 V *versus* K/K^+ predicted according to the theoretical model and DFT calculation. (b) The minimum Gibbs free energy of adsorption *versus* descriptor. (c) The capacitance of the unit charge storage site *versus* descriptor at a potential U of 0.7 V and 1.0 V for Na and K, respectively. (d) Measured specific capacitance from electrochemical measurements, normalized by the undoped pure carbon-based electrode in an alkaline (KOH) electrolyte under the same conditions in the same experiment (Table S6†). The predicted specific capacitance according to theoretical models, normalized using undoped graphene, is also plotted against the descriptor.

the specific surface area is accounted for in the calculations of specific capacitances (capacitance per unit area). The specific capacitances were then normalized using the specific capacitance of the undoped graphene electrode, measured under the same conditions in the same experiments. Although the morphology of the materials and dopant content could also affect the specific capacitances, since only graphene and some nanocarbon spheres were selected, their morphology and dopant content were similar and comparable. To further minimize the possible surface area/morphology/dopant content effects, we have averaged the data that were carefully selected from the literature.

The theoretically computed specific capacitance of the X-G was also normalized to that of undoped graphene and compared with the experimental data. Fig. 5d shows the normalized capacitances as a function of the descriptor for the X-G. Both DFT calculation and the experimental results show a volcano relationship with nitrogen sitting on the top, which agrees well with the predictions of the theoretical model. Thus, the descriptor provides a theoretical tool to predict the energy storage capacity of the X-G, from which the best electrode materials could be selected.

The predictive power of the descriptor Φ mainly originates from the intrinsic physical meaning that correlates the properties with the structure of active sites, as mentioned in our previous study.[36] In terms of the definition of Pauling and Mulliken, the electric potential for an electrode μ depends strongly on its electronegativity and can be expressed as $\mu \approx -\chi_M$, where χ_M is the Pauling and Mulliken electronegativity. From the perspective of the external circuit, the increased electric potential results from accumulation of more and more electrons, which will lead to the relationship $eU = \mu(N+1) - \mu(N)$ for each added electron, where $\mu(N)$ and $\mu(N+1)$ denote the chemical potential of the electrode (here, it is doped graphene) with N-electrons and $(N+1)$-electrons at the ground state. Finally, at the ground state, capacity can be derived from electronegativity or our descriptor using

$$C_{0/\text{site}} = \frac{e^2}{\chi_M(N) - \chi_M(N+1)}$$

based on the definition of capacitance. Consequently, the capacitance directly relies on the electronegativity. The dual-volcano-shaped relationship probably originates from the difference in doping sites. As shown in Fig. 1a and Table S4 (ESI†), the doped structures are quite different: on the left side of N, including N, dopants are embedded into the graphene lattice to form sp^2 chemical bonds with two and even three carbon atoms, but on the right side of N, most dopants can only attach on the edge of graphene or adsorb on the surface of graphene by grafting. Thus, the doping structures can be identified from the descriptor and provide an insight into the charge storage mechanism.

Simultaneous improvement of both capacity and rate by dual-element doping

According to the predictions of the above volcano relationship and charge storage origin, there is still large room for us to improve the capacitance towards the ideal charge storage capacity corresponding to the zero charge storage energy barrier (Fig. 5b). Here, a strategy of co-doping is used to further increase the charge storage capacity. Since N is the best dopant among the p-orbital elements, it is selected to combine with the dopants S and F to form N, S and N, F co-doped graphene structures to store Na and K (Fig. 6a). ΔG^{min}_{Na*} and ΔG^{min}_{K*} were determined using the same method as single-element doping (Fig. 6b). As expected, ΔG^{min}_{Na*} and ΔG^{min}_{K*} can be further reduced by co-doping, and the capacity of the anode in SIBs and KIBs can be pushed to its limit (Fig. 6d–f). These predictions are consistent with the experimental results.[41,42] The improved capacity can be attributed to the synergistic effect originating from the valence electron interactions between dopants.[43] Here, it should be noted that the predicted specific capacitance should be larger than that in the electrochemical experiment in general based on ideal conditions, but it is actually smaller. This discrepancy results from the fact that the ideal adsorption of monolayer metal ions was defined as the pseudocapacitive mechanism in our DFT calculation, but in

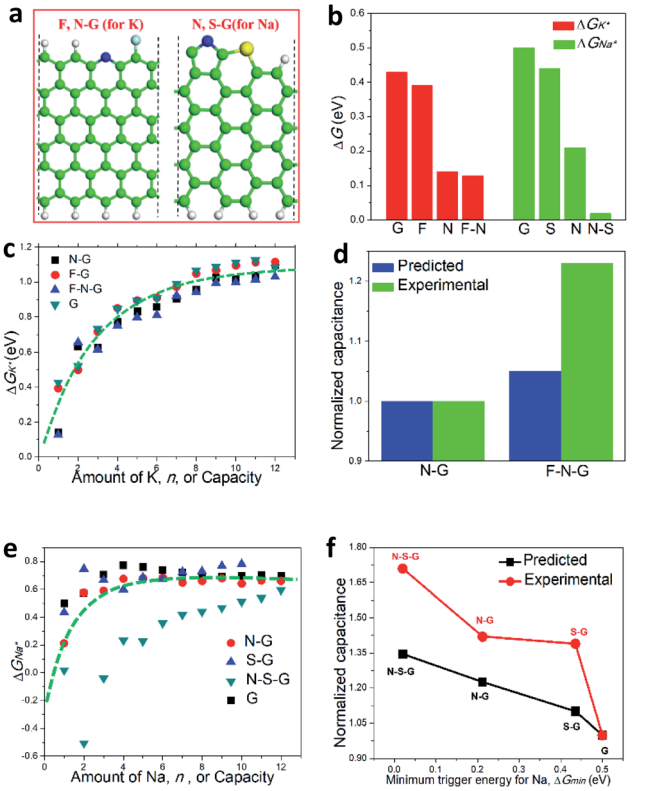

Fig. 6 (a) The selected optimal models of F, N-codoped graphene for K storage and N, S-codoped graphene for Na storage among all 30 possible codoped models. (b) The minimum Gibbs free energy ΔG_{min} for Na and K adsorption on corresponding mono- and multi-doped graphene models. (c) The comparison between change of Gibbs free energy for F, N-codoped and mono-doped graphene models adsorbing K. (d) The comparison between predicted capacitance and experimental data for K storage by normalization.[41] (e) The comparison between the change of Gibbs free energy for N, S-codoped and mono-doped graphene models adsorbing Na. (f) The comparison between predicted capacitance and experimental data for Na storage by normalization.[42]

the experiment, the electrode material surface may adsorb more than one metal deposition layers. Deposition of the additional layers is possible, as predicted in Fig. 4b, resulting in higher capacitive capacity. In addition, more ions may also be stored in the gaps between the reduced graphene layers but the mechanism should be classified as the ion battery mechanism rather than the pseudocapacitive mechanism. Anyway, both experimental results and predictions show that the capacitive performance of dual-element doping is indeed higher than that of single one.

We have calculated the upper limit of the capacity of the doped graphene anode based on the charge storage mechanism. In fact, the charge process of the heteroatom-doped carbon anode in SIBs and KIBs is the process in which several energy barriers must be overcome by the applied external electric potential.[36] These include (i) the thermodynamics energy barrier for adsorption (*i.e.*, ΔG_{Na*} and ΔG_{K*} in this study), (ii) the energy barrier due to adsorbate interaction determined by the intrinsic properties of adsorbates such as the atomic radius, electronegativity, electron affinity, charge carried by ions, *etc.*, (iii) the energy barrier originating from thermal motion being represented by k_BT, and (iv) the phase transition energy barrier ΔG_T mainly relying on the adsorbed ion itself. Therefore, even if the adsorption energy barrier ΔG_{Na*} (or ΔG_{K*}) is reduced to zero by doping, other energy barriers cannot be eliminated, let alone the existence of external resistance, as shown in Fig. 6c–e. Thermodynamically, the zero adsorption energy barrier ΔG_{Na*} (or ΔG_{K*}) corresponds to the upper limit of $C_{0/site} = e/[U(1 + \exp(-eU/k_BT)) \approx e/U$ for $eU \gg k_BT$. Therefore, the capacity depends only on electric potential for a single site under the zero energy barrier. The capacitance per unit charge storage site at the atomic level is different from the macroscopic capacitance that is independent of the amount of charge added to the system and relies only on geometrical parameters of the system as well as the dielectric constant.

In addition to the improved energy density (capacitance), the doping could further improve the power density (or rate). For a given external condition such as ohmic resistance, C^+ diffusion, conductivity and charging potential in a charging system, the rate of Na and K storage in surface-dominated anodes is mainly governed by the chemisorption rate of cations, and can be written as

$$P_{0/site} = k_0 \times \frac{eUk_BT \ln\left[\frac{1}{2}\left(1 + e^{\frac{eU - \Delta G^{min}_{C*}}{k_BT}}\right)\right] - \frac{1}{2}\left(\Delta G^{min}_{C*} - eU\right)^2}{\Delta G^{max}_{C*} - \Delta G^{min}_{C*} + k_BT\left(e^{\frac{\Delta G^{max}_{C*} - eU}{k_BT}} + e^{\frac{\Delta G^{min}_{C*} - eU}{k_BT}}\right)} \quad (4)$$

where k_0 and k_B are the rate constant and the Boltzmann constant, respectively (see the details in the ESI†). According to eqn (4), the charging rate not only depends on the intrinsic factors such as the doping structures, but also relies on the extrinsic factors including charging potential U, electrolytes and pH value. For a given charging system, the doping generally enhances the power density and capacity, depending on the types of dopants, as illustrated in Fig. 7 and S10 (ESI†). Overall, according to eqn (4) and (S19) (ESI†), doping would reduce ΔG^{min}_{C*}, which would enhance both energy density and power density simultaneously for SIBs and KIBs based on the pseudocapacitive mechanism.

Discussion

We have performed DFT calculations to understand the origin of the X-G-based anode materials for surface-dominated SIBs and KIBs and discovered an intrinsic descriptor that describes the energy storage capacity and rate of the anode materials well. On the basis of the above results, both the energy and power densities are determined by intrinsic and extrinsic factors associated with active sites. As the adsorption occurs only on the active sites, the charge storage activity of the X-G is directly related to the unit activity of the active sites (intrinsic factor), while the population of exposed active sites for a given electrode mass in energy devices is the extrinsic factor, which is related to the density of exposed active sites and the specific surface area (Sc). According to eqn (3) and (4), in addition to the intrinsic and extrinsic factors, environmental factors (*e.g.*, U and pH) also affect the proton adsorption of the electrodes. From the above analysis, anode material design strategies can be established to achieve these predicted structures or functions by considering the intrinsic and extrinsic factors as well as the environmental factors. These strategies include:

(i) Creating highly-effective active sites. This anode material design strategy is used to enhance the intrinsic activity of active centers (intrinsic factors). Doping using p-block dopants with $0.5 < Ø < 1.5$ and $2.5 < Ø < 3.5$ and introducing more edges based on the edge effect could significantly enhance the charge storage capacity. Co-doping, such as N, S and F, N co-doping, could further enhance the storage capacity due to the synergetic effect, as shown in Fig. 6a and b.

(ii) Building 3D nanoarchitectures to expose more active sites. This materials design strategy is used to populate more active sites on the electrode surfaces (extrinsic factors). 3D porous carbon or nanoarchitectured electrodes could have a large specific-surface area to facilitate ion diffusion as well as increasing the number of exposed active sites. As illustrated in Fig. S9 (ESI†), the effective area could be increased by a factor of 2–10 by introducing carbon nanotube pillars, C_{60} and wrinkles

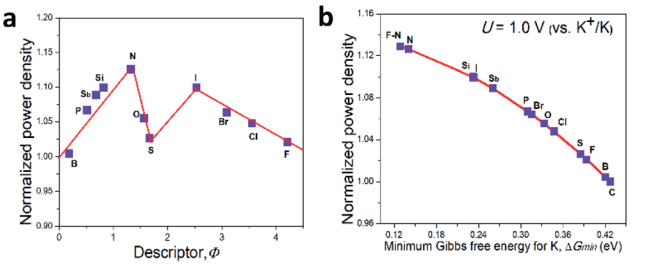

Fig. 7 (a) Normalized power per unit site by undoped graphene *versus* descriptor $Φ$. (b) Normalized power per unit site by undoped graphene *versus* minimum K adsorption energy ΔG^{min}_{K*} at a given potential of U = 1.0 V.

on the graphene surface. Of course, for a general battery, this will be an optimization problem that needs to balance the energy and power densities, especially for the development of lightweight and miniaturized electronic devices.

(iii) Multilayer storage of Na and K ions on doped graphene surfaces. According to the analysis, the layers of Na and K atoms grow along the (110) crystallographic plane of the Na and K crystals because of the fine in-plane lattice matching between Na and K and the graphene substrate, resulting in planar Na and K deposition. Thus, multilayer storage of Na and K ions on the doped graphene surface is possible without introducing dendritic structures, which could significantly increase the cycling performance and specific energy and power densities.

(iv) Optimization of the width of the interlayer gap. A wider interlayer gap is beneficial for transportation of sodium or potassium ions, further leading to high rate capability, or power density. However, a three-dimensional anode material, or a bulk anode, cannot be used effectively. In addition, the width of interlayer gaps can result in the formation of a diffusion layer along the radial direction, which is ineffective in enhancing the capacity. On the other hand, cations are not easy to transfer in the deeper interlayer gap, leading to higher diffusion overpotential. Overall, the ratio of the length to the radius ($\chi = L/d$) for the interlayer gap of anode materials should be optimized reasonably. Thus, an ideal doping method with multiple dopants beyond dual doping can be used to reduce the energy barrier to zero, leading to an ideal capacitive performance for a given external condition. As mentioned above, for the zero energy barrier, capacitance per unit site can be given by $C_{0/\text{site}} = e/[U(1 + \exp(-eU/k_BT)) \approx e/U$ for $eU \gg k_BT$. Accordingly, for the same external electric potential U as shown in Table S4 (ESI†), this ideal capacitance will be 1.43 e per V per site for sodium adsorption, which is almost 13 times larger than that of the N, S co-doped graphene anode, and 1 e per V per site for potassium storage with a factor of 4.7 compared with that of the F, N co-doped anode. Obviously, there is still a lot of room for improvement of the capacitance by the heteroatom-doping strategy.

Conclusions

The charge/discharge processes on heteroatom-doped graphene anode materials in SIBs and KIBs were analyzed with the DFT method. The Gibbs free energy of adsorption, the capacity, and the energy and power densities were calculated to understand the origin of charge storage on the doped carbon surfaces. The results show that doping can significantly lower the Gibbs free energy of adsorption and consequently enhance both energy and power densities. Co-doping can even further improve the charge storage capabilities due to the synergistic effect between the dopants. Introducing more graphene edges could also significantly enhance the charge storage capacity. A descriptor correlating charge storage capabilities with the doping structures was discovered, from which the optimal electrode structures could be predicted. In addition, the graphene substrate can guide the preferential growth of K and Na during the long-term and repeated electrodeposition process, which could inhibit dendrite development effectively. Such a design principle provides a critical guidance for rational design of carbon-based electrodes for high-performance supercapacitors.

Methods

Simulation methods

The adsorption of sodium ions in a neutral electrolyte and potassium ions in an alkaline electrolyte during the charge process of SIBs and KIBs on various heteroatom-doped graphene surfaces was studied using density functional theory (DFT) with spin polarization, as implemented in the Vienna *ab initio* Simulation Package (VASP) code. The projector augmented wave (PAW) pseudo-potentials were used to describe nucleus–electron interactions, while the electronic exchange and correlation effects were modelled using the Perdew–Burke–Ernzerhof functional within the generalized gradient approximation (GGA). For the plane wave basis set, a high kinetic energy cutoff of 400 eV was selected after testing several different cutoff energies. 10^{-5} eV was used as the convergence criterion of the electronic structure iteration. For geometry optimization, the convergence criterion for the force of the system was set to about 0.01 eV Å^{-1}. The *K*-points were set to $4 \times 4 \times 1$ and $4 \times 1 \times 1$ for graphene sheet models and graphene nanoribbon models, respectively. The choice of the k point mesh and cutoff energy was able to ensure that energies converged to about 1 meV per atom.

Three different groups of graphene models were developed to explore the adsorption effects of electrolyte ions in the charge process. The first group of graphene models is periodic in the *x*- and *y*-directions, consisting of 48 carbon atoms. The second group of models is armchair graphene nanoribbons consisting of 36 carbon atoms and 8 hydrogen atoms used to saturate hanging bonds at the edges of graphene. The third group of models is zigzag graphene nanoribbons comprising 48 carbon atoms and 8 hydrogen atoms. Both armchair and zigzag nanoribbons were constructed as a three-dimensional periodic structure with vacuum layers around 14 Å and 18 Å in the *y*- and *z*-directions, respectively, to avoid interaction between graphene slabs.

Experimental methods

The rGO substrates were prepared according to our previous work.[38] The Na metal and K metal used for asymmetric cells were prepared by rolling the Na/K into thin foil pieces (0.5 mm in thickness) and then punching them into 12 mm-diameter disks. CR2032 coin cells were employed for Na/K deposition testing. The electrolytes used for rGO|Na and rGO|K asymmetric cells were 1.0 M $NaClO_4$ in a mixed solvent of EC and DEC (1 : 1 in volume) and 1.0 M KPF_6 in a mixed solvent of EC and DEC (1 : 1 in volume), respectively. Whatman glass microfiber was used as the separator. All the cells were assembled in an argon-filled glovebox with the concentrations of moisture and oxygen below 0.1 ppm and were tested using a CT2001A cell test instrument (LAND Electronic Co, BT2013A, China) or an 88-channel battery tester (Arbin Instruments, BT2000, USA).

Conflicts of interest

There are no conflicts to declare.

Acknowledgements

This work was supported financially by the National Natural Science Foundation of China (51704243), the Fundamental Research Funds for the Central Universities (3102019ZD0402) and the Innovation Foundation for Doctor Dissertation of Northwestern Polytechnical University (CX201943). ZX thanks the U.S. National Science Foundation (1662288) for the financial support.

Notes and references

1 M. D. Slater, D. Kim, E. Lee and C. S. Johnson, *Adv. Funct. Mater.*, 2013, **23**, 947.
2 J. T. Xu, M. Wang, N. P. Wickramaratne, M. Jaroniec, S. X. Dou and L. M. Dai, *Adv. Mater.*, 2015, **27**, 2042.
3 V. L. Chevrier and G. Ceder, *J. Electrochem. Soc.*, 2011, **158**, A1011.
4 P. Barpanda, G. Oyama, S. Nishimura, S. C. Chung and A. Yamada, *Nat. Commun.*, 2014, **5**, 4358.
5 H. W. Lee1, R. Y. Wang, M. Pasta1, S. W. Lee, N. Liu and Y. Cui, *Nat. Commun.*, 2014, **5**, 5280.
6 V. Palomares, P. Serras, I. Villaluenga, K. B. Hueso, J. Carretero-Gonzalez and T. Rojo, *Energy Environ. Sci.*, 2012, **5**, 5884.
7 S. W. Kim, D. H. Seo, X. H. Ma, G. Ceder and K. Kang, *Adv. Energy Mater.*, 2012, **2**, 710.
8 J. Xu, S. L. Chou, J. L. Wang, H. K. Liu and S. X. Dou, *ChemElectroChem*, 2014, **1**, 371.
9 K. B. Hueso, M. Armand and T. Rojo, *Energy Environ. Sci.*, 2013, **6**, 734.
10 P. Moreau, D. Guyomard, J. Gaubicher and F. Boucher, *Chem. Mater.*, 2010, **22**, 4126.
11 W. L. Zhang, F. Zhang, F. W. Ming and H. N. Alshareef, *EnergyChem*, 2019, **1**, 100012.
12 B. Jache and P. Adelhelm, *Angew. Chem., Int. Ed.*, 2014, **53**, 10169.
13 Y. Wen, K. He, Y. J. Zhu, F. D. Han, Y. H. Xu, I. Matsuda, Y. Ishii, J. Cumings and C. S. Wang, *Nat. Commun.*, 2014, **5**, 4033.
14 H. S. Hou, Y. C. Yang, Y. R. Zhu, M. J. Jing, C. C. Pan, L. B. Fang, W. X. Song, X. M. Yang and X. B. Ji, *Electrochim. Acta*, 2014, **146**, 328.
15 S. Huang, C. Meng, M. Xiao, S. Ren, S. J. Wang, D. M. Han, Y. N. Li and Y. Z. Meng, *Sustainable Energy Fuels*, 2017, **1**, 1944.
16 J. Park, J. W. Park, J. H. Han, S. W. Lee, K. Y. Lee, H. S. Ryu, K. W. Kim, G. X. Wang, J. H. Ahn and H. J. Ahn, *Mater. Res. Bull.*, 2014, **58**, 186.
17 J. F. Qian, D. Qiao, X. P. Ai, Y. L. Cao and H. X. Yang, *Chem. Commun.*, 2012, **48**, 8931.
18 L. Wang, X. M. He, J. J. Li, W. T. Sun, J. Gao, J. W. Guo and C. Y. Jiang, *Angew. Chem., Int. Ed.*, 2012, **51**, 9034.
19 C. Marino, A. Debenedetti, B. Fraisse, F. Favier and L. Monconduit, *Electrochem. Commun.*, 2011, **13**, 346.
20 J. Sun, H. W. Lee, M. Pasta, H. T. Yuan, G. Y. Zheng, Y. M. Sun, Y. Z. Li and Y. Cui, *Nat. Nanotechnol.*, 2015, **10**, 1038.
21 L. W. Jiang, Y. X. Lu, C. L. Zhao, L. L. Liu, J. N. Zhang, Q. Q. Zhang, X. Shen, J. M. Zhao, X. Q. Yu, H. Li, X. J. Huang, L. Q. Chen and Y. S. Hu, *Nat. Energy*, 2019, **4**, 495.
22 R. J. Gummow, G. Vamvounis, M. B. Kannan and Y. H. He, *Adv. Mater.*, 2018, **30**, 1801702.
23 M. C. Lin, M. Gong, B. Lu, Y. Wu, D.-Y. Wang, M. Guan, M. Angell, C. Chen, J. Yang, B. J. Hwang and H. Dai, *Nature*, 2015, **520**, 324.
24 C. Xu, Y. Chen, S. Shi, J. Li, F. Kang and D. Su, *Sci. Rep.*, 2015, **5**, 14120.
25 D. D. Li, L. Zhang, H. B. Chen, J. Wang, L. X. Ding, S. Q. Wang, P. J. Ashmanb and H. H. Wang, *J. Mater. Chem. A*, 2016, **4**, 8630.
26 Y. Yan, Y. X. Yin, Y. G. Guo and L. J. Wan, *Adv. Energy Mater.*, 2014, 1301584.
27 S. Huang, C. Meng, M. Xiao, S. Ren, S. J. Wang, D. M. Han, Y. N. Li and Y. Z. Meng, *Small*, 2018, **14**, 1704367.
28 Y. Wang, C. Y. Wang, Y. J. Wang, H. K. Liu and Z. G. Huang, *ACS Appl. Mater. Interfaces*, 2016, **8**, 18860.
29 P. Z. Wang, B. Qiao, Y. C. Du, Y. F. Li, X. S. Zhou, Z. H. Dai and J. C. Bao, *J. Phys. Chem. C*, 2015, 119.
30 Z. H. Wang, L. Qie, L. X. Yuan, W. X. Zhang, X. L. Hu and Y. H. Huang, *Carbon*, 2013, **55**, 328.
31 H. S. Hou, L. Shao, Y. Zhang, G. Q. Zou, J. Chen and X. B. Ji, *Adv. Sci.*, 2017, **4**, 1600243.
32 L. Qie, W. M. Chen, X. Q. Xiong, C. C. Hu, F. Zou, P. Hu and Y. H. Huang, *Adv. Sci.*, 2015, **2**, 1500195.
33 C. Ling and F. Mizuno, *Phys. Chem. Chem. Phys.*, 2014, **16**, 10419.
34 D. Datta, J. W. Li and V. B. Shenoy, *ACS Appl. Mater. Interfaces*, 2014, **6**, 1788.
35 Y. Y. Liu, V. I. Artyukhov, M. J. Liu, A. R. Harutyunyan and B. I. Yakobson, *J. Phys. Chem. Lett.*, 2013, **4**, 1737.
36 Y. Gao, J. Zhang, X. Luo, Y. Wan, Z. Zhao, X. Han and Z. H. Xia, *Nano Energy*, 2020, **72**, 104666.
37 V. Palomares, P. Serras, I. Villaluenga, K. B. Hueso, J. Carretero-Gonzalez and T. Rojo, *Energy Environ. Sci.*, 2012, **5**, 5884.
38 N. Li, K. Zhang, K. Xie, W. F. Wei, Y. Gao, M. H. Bai, Y. L. Gao, Q. Hou, C. Shen, Z. H. Xia and B. Q. Wei, *Adv. Mater.*, 2019, 1907079.
39 D. C. Lin, Y. Liu, Z. Liang, H. W. Lee, J. Sun, H. T. Wang, K. Yan, J. Xie and Y. Cui, *Nat. Nanotechnol.*, 2016, **10**, 1038.
40 Z. H. Zhao, M. T. Li, L. P. Zhang, L. M. Dai and Z. H. Xia, *Adv. Mater.*, 2015, **27**, 6834.
41 J. S. Zhou, J. Lian, L. Hou, J. C. Zhang, H. Y. Gou, M. R. Xia, Y. F. Zhao, T. A. Strobel, L. Tao and F. M. Gao, *Nat. Commun.*, 2015, **6**, 8503.
42 K. Gopalsamy, J. Balamurugan, T. D. Thanh, N. H. Kim and J. H. Lee, *Chem. Eng. J.*, 2017, **312**, 180.
43 S. Bag, B. Mondal, A. K. Das and C. R. Raj, *Electrochim. Acta*, 2015, **163**, 16.

